THE UNIVERSITY *of* EDINBURGH

Edinburgh Research Explorer

Boundary conditions for simulations of oscillating bubbles using the non-linear acoustic approximation

OPEN ACCESS

Boundary conditions for simulations of oscillating bubbles using the non-linear acoustic approximation

J. R. C. King[a,*], A. M. Ziolkowski[a], M. Ruffert[b]

[a] *University of Edinburgh, School of GeoSciences, Grant Institute, The King's Buildings, James Hutton Road, Edinburgh, EH9 3FE, UK.*
[b] *University of Edinburgh, School of Mathematics & Maxwell Institute, JCMB, The King's Buildings, Peter Guthrie Tait Road, Edinburgh, EH9 3FD, UK.*

Abstract

We have developed a new boundary condition for finite volume simulations of oscillating bubbles. Our method uses an approximation to the motion outside the domain, based on the solution at the domain boundary. We then use this approximation to apply boundary conditions by defining incoming characteristic waves at the domain boundary. Our boundary condition is applicable in regions where the motion is close to spherically symmetric. We have tested our method on a range of one- and two-dimensional test cases. Results show good agreement with previous studies. The method allows simulations of oscillating bubbles for long run times (5×10^5 time steps with a CFL number of 0.8) on highly truncated domains, in which the boundary condition may be applied within 0.1% of the maximum bubble radius. Conservation errors due to the boundary conditions are found to be of the order of 0.1% after 10^5 time steps. The method significantly reduces the computational cost of fixed grid finite volume simulations of oscillating bubbles. Two-dimensional results demonstrate that highly asymmetric bubble features, such as surface instabilities and the formation of jets, may be captured on a small domain using this boundary condition.

Keywords: boundary condition, non-linear acoustic approximation, underwater explosion, oscillating bubble, ghost fluid method

*Tel: +44 (0) 131 650 5916
Email address: `j.r.c.king@ed.ac.uk` (J. R. C. King)

1. Introduction

Many problems in fluid dynamics are posed in unbounded domains. Various methods are employed to enable these problems to be solved numerically, a common one of which is to restrict the computation to a finite region and impose artificial boundary conditions on the truncated domain. The aim of the artificial boundary conditions is to mimic the unbounded domain and prevent spurious reflections from the domain boundary. Artificial boundary conditions of this type are often referred to as 'non-reflecting' and 'absorbing'. Inaccurate absorbing boundary conditions can lead to spurious disturbances at the domain boundaries, which propagate back through the domain, contaminating results.

There has been much work on non-reflecting boundary conditions. Reviews have been provided by Givoli [1], Hagstrom [2] and Tsynkov [3]. Many methods have been derived for wave propagation problems, such as the perfectly matched layer method [4, 5] which are only strictly applicable to linear hyperbolic systems. However similar methods for the Euler equations have been developed [6]. A good review of work on artificial boundary conditions for compressible flow is given by Colonius [7].

Hedstrom [8] decomposed the Euler equations into characterstic wave equations and presented a non-reflecting boundary condition using these equations. Thompson [9] developed a useful formalism for applying characteristic boundary conditions, and described a method of applying non-reflecting characteristic boundary conditions [10]. The characteristic boundary condition formalism of [9] is widely used.

The behaviour of oscillating air bubbles in water is of interest in a variety of fields, including cavitation, underwater explosions, and shock wave lithotripsy. In 1917, Rayleigh [11] developed an equation of motion for a spherical cavity in an infinite incompressible fluid. The analysis in [11] forms the basis for much work on oscillating bubbles. Lamb [12] derived an exact wave equation for the motion of a spherical cavity in a compressible fluid, and obtained an analytical solution for the special case of the ratio of specific heats, γ, being equal to $4/3$. In general there is no analytical solution to this equation. Extensions to [11] accounting for the compressibility of water were developed by several authors [13, 14]. Gilmore [15] developed the work of [11, 12, 13] to obtain an algorithm to calculate the propagating wavefield outside the bubble. This scheme requires further approximations, and is less accurate than the equations of motion on which it is based. Although on a

much smaller scale, cavitation bubbles are a physically similar phenomenon, and similar approximations have been developed to describe cavitation bubbles [16, 17], leading to the widely used Rayleigh-Plesset equation. Further analysis of this form of approximation was carried out in [18, 19].

Marine seismic exploration can be thought of as a powerful form of echo sounding, capable of penetrating the sea floor, to enable a three-dimensional image of the sub-sea to be created. It is a process used in the petroleum industry in the search for geological features which have the potential to contain trapped hydrocarbons. Initially dynamite was used as the source in marine seismic exploration. However environmental concerns led to the development of alternative sources. Currently, seismic air guns are the most commonly used source. In use they are towed behind a ship, usually between 5 and 20 metres beneath the sea surface, and when 'fired' release a quantity of air at high pressure (136 atm), that forms a bubble which oscillates, producing a wavefield which propagates through the sea and into the subsurface. A seismic air gun is analagous to a weak underwater explosion.

Air gun bubbles were first modelled in 1970 by Ziolkowski [20], using a simplified two-equation ordinary differential equation model of a seismic air gun based on the work of [15]. This method is still the basis of the modelling currently used by industry. The non-linear acoustic approximation (NLAA) was developed by Ziolkowski [21] as an improvement to [20], and is equivalent to the approximations of [13, 14]. The NLAA approximates the wavefield produced by an oscillating bubble - subject to certain assumptions - and allows the calculation of pressure and velocity at any point provided the pressure and velocity are known at a single location. Boundary integral methods which allowed the simulation of non-spherical bubbles have been developed for cavitation modelling [22, 23, 24]. Cox et al. [25] provide a good review of air gun modelling, and apply earlier boundary integral methods to seismic air guns.

The first finite volume simulations of underwater explosions appear in [26], although a lack of adequate boundary conditions mean that only very early stages of the explosion were calculated. A review of early work on underwater explosions is provided in [27]. The one-dimensional spherically symmetric underwater explosion has since become a commonly used test case (although no analytical solution exists) for multimedium Euler solvers, and has been simulated using a variety of numerical schemes [28, 29, 30, 31, 32, 33]. In a typical underwater explosion problem the outgoing pressure wavefield propagates to approximately 100 times the maximum bubble radius during a single

3

bubble oscillation. Previous simulations have relied either on the use of a very large domain (for example [33]) which is computationally expensive, or on arbitrary Lagrangian-Eulerian methods [29, 30, 31] in which the problem is solved on a mesh which expands to contain the outgoing wavefield.

Our solution is to take the non-linear acoustic approximation and use it to develop artificial boundary conditions for a finite volume simulation of an oscillating bubble on a truncated domain. We base our approximation on the conditions at the domain boundary. This approximation is then used to describe any incoming characteristic waves. These characteristic waves are then applied through the characteristic boundary condition formalism of [9]. This method allows finite volume simulations of oscillating bubbles to be carried out for long run times on comparatively small domains, reducing computational costs. We present our theory in two dimensions, and provide one- and two-dimensional results, although the theory could be applied to three-dimensional simulations.

The layout of the paper is as follows. In Section 2 we show the derivation of the NLAA. In Section 3 we present a brief summary of the characteristic boundary condition formalism and use the NLAA to derive artificial boundary conditions. In Section 4 we describe the numerical scheme in which we implement our boundary conditions. In Section 5 we present the results of some one-dimensional test cases using our new method, and discuss the performance of the method. In Section 6 we present results from two-dimensional simulations. Section 7 is a summary of conclusions.

2. The non-linear acoustic approximation

Ziolkowski [21] developed the non-linear acoustic approximation for the motion of a spherical bubble in water for use in modelling seismic air guns. The approximation is based on the assumption that the acoustic wavefield produced by the bubble is dominated by wavelengths many times the bubble diameter, which allows the bubble to be considered a monopole source. The velocity is described by a velocity potential which is assumed to obey the linear acoustic wave equation, leading to an analytical solution for the velocity potential. This solution is then passed back into the Euler equations to obtain solutions for the pressure and velocity. The following is the derivation from [21]. We include this derivation as we will refer to several of the equations frequently in the following sections of this paper, and wish to avoid cumbersome citations to facilitate flow of exposition.

4

Starting from Lamb [12], the bubble is assumed to be spherical, and all motion is in the radial direction and subject to spherical symmetry. The local specific enthalpy in the water, h, is defined as

$$h = \int_{p_\infty}^{p} \frac{dp}{\rho} = \int_{\rho_\infty}^{\rho} c^2 \frac{d\rho}{\rho},$$ (1)

where p is the pressure, ρ is the density, and c is the speed of sound, defined by $c^2 = \frac{dp}{d\rho}\Big|_{isentropic}$. p_∞ and ρ_∞ are the pressure and density in the undisturbed water. For the pressure fluctuations considered, it is acceptable to assume that $\rho = \rho_\infty$ and $h = (p - p_\infty)/\rho_\infty$. The speed of sound in the water is assumed to be constant. It should be noted that this combination of assumptions - incompressible flow and finite speed of sound - is a contradictory set of assumptions, but acceptable because of the low Mach number flows involved. Viscosity is neglected [20]. The flow is assumed to be irrotational and the velocity $\mathbf{u} = u\mathbf{e_r}$ obeys a velocity potential such that $\mathbf{u} = -\nabla\phi$. Hence $u = -\frac{\partial\phi}{\partial r}$. The equation of motion is written

$$\frac{D\mathbf{u}}{Dt} + \nabla h = 0,$$ (2)

where $\frac{D(\cdot)}{Dt}$ is the material derivative, defined by $\frac{D(\cdot)}{Dt} = \frac{\partial(\cdot)}{\partial t} + u\nabla(\cdot)$. Equation 2 is integrated to give

$$h = \frac{\partial\phi}{\partial t} - \frac{u^2}{2}.$$ (3)

An equation for the conservation of mass is written

$$\frac{1}{\rho}\frac{D\rho}{Dt} - \nabla^2\phi = 0.$$ (4)

Equations 1 and 4 are combined to obtain

$$\frac{Dh}{Dt} = \frac{c^2}{\rho}\frac{D\rho}{Dt} = c^2\nabla^2\phi.$$ (5)

With the imposition of spherical symmetry, from equations 3 and 5 the exact wave equation, first derived in [12], is obtained

$$\frac{\partial^2\phi}{\partial r^2}\left(1 - \frac{u^2}{c^2}\right) + \frac{2}{r}\frac{\partial\phi}{\partial r}\left(1 + \frac{r}{c^2}\frac{\partial^2\phi}{\partial t\partial r}\right) - \frac{1}{c^2}\frac{\partial^2\phi}{\partial t^2} = 0.$$ (6)

5

Equation 6 has no known analytical solution. If the advective terms - $u\frac{\partial(\cdot)}{\partial r}$ - in equations 2, 4 and 5 are neglected the linear acoustic wave equation in ϕ is obtained

$$\frac{\partial^2 \phi}{\partial r^2} + \frac{2}{r}\frac{\partial \phi}{\partial r} - \frac{1}{c^2}\frac{\partial^2 \phi}{\partial t^2} = 0. \tag{7}$$

Lamb [12] estimated that for flows with Mach number less than approximately 0.1, the errors caused by this approximation would be less than 1%. The wavelengths of the pressure field produced by the bubble are large compared with the bubble radius, hence the bubble can be considered a point source. There are no other sources. Under these conditions, equation 7 has the well known solution

$$\phi(r, t) = \frac{1}{r}f\left(t - \frac{r}{c}\right). \tag{8}$$

Differentiation of equation 8 yields

$$u(r, t) = -\frac{\partial \phi}{\partial r} = \frac{1}{r^2}f + \frac{1}{rc}f' \tag{9}$$

where the argument of f, $(t - r/c)$, has been dropped for ease of writing, and a prime denotes differentiation with respect to the argument. Further differentiation gives

$$\frac{\partial u}{\partial r} = -\frac{\partial^2 \phi}{\partial r^2} = \frac{-2}{r^3}f - \frac{2}{r^2 c}f' - \frac{1}{rc^2}f'' \tag{10}$$

and

$$\frac{\partial u}{\partial t} = -\frac{\partial^2 \phi}{\partial r \partial t} = \frac{1}{r^2}f' + \frac{1}{rc}f''. \tag{11}$$

These results are passed into equations 2 and 4 giving

$$\frac{1}{r^2}f' + \frac{1}{rc}f'' + \frac{1}{\rho}\frac{\partial p}{\partial r} + u\left(\frac{-2}{r^3}f - \frac{2}{r^2 c}f' - \frac{1}{rc^2}f''\right) = 0. \tag{12}$$

Equations 3, 8, 9 and 11 are used to provide expressions for f, f' and f''

$$f = r^2\left(u - \frac{h}{c} - \frac{u^2}{2c}\right), \tag{13}$$

$$f' = r\frac{\partial \phi}{\partial t} = r\left(h + \frac{u^2}{2}\right), \tag{14}$$

6

$$f'' = rc\frac{\partial u}{\partial t} - ch - \frac{cu^2}{2}. \tag{15}$$

Ziolkowski [21] argues that the quantity $r\left(h + u^2/2\right)$ propagates outwards at speed c with uniform amplitude, and determines a Lagrangian form of this result, obtaining

$$R\ddot{R}\left(1 - \frac{2\dot{R}}{c}\right) + \frac{3\dot{R}^2}{2}\left(1 - \frac{4\dot{R}}{3c}\right) = H + \frac{R\dot{H}}{c}\left(1 - \frac{\dot{R}}{c}\right), \tag{16}$$

where R is the bubble radius, H the enthalpy of the water at the bubble wall, c the speed of sound of water. A dot represents differentiation with respect to time. This result is solved numerically along with an equation such as $PR^{3n} = constant$, where n is a constant and $1 \leq n \leq 1.4$ [20], to simulate the evolution of the bubble through time. P and R are also used with the above results to calculate an approximation of the pressure and velocity at any point in the water.

3. Definition of boundary conditions using the non-linear acoustic approximation

3.1. Characteristic boundary condition formalism

Consider a finite spherical domain Ω, of radius R_D, bounded by Γ. Ω is centred on the origin of a polar coordinate system, subject to polar axisymmetry, in which r is the radial distance and θ the polar angle. Thompson [9] presents a formalism for the treatment of boundary conditions in finite difference simulations for hyperbolic systems of conservation laws. This method decomposes of the system of equations into a set of uncoupled wave equations for non-linear characteristics. This set of equations is then solved on domain boundaries, with any incoming characteristic waves being specified according to the boundary condition desired. Starting from the Euler equations for primitive variables density ρ, pressure p, radial velocity u and polar velocity v, in polar coordinates, the uncoupled wave equations for non-linear characteristics on Γ may be written as

$$\frac{\partial \rho}{\partial t} + \frac{1}{c^2}\left\{\mathscr{L}_2 + \frac{1}{2}\left[\mathscr{L}_4 + \mathscr{L}_1\right]\right\} + \frac{2\rho u}{r} + \frac{v}{r}\frac{\partial \rho}{\partial \theta} + \frac{\rho}{r}\frac{\partial v}{\partial \theta} + \frac{\rho v}{r\tan\theta} = 0, \tag{17}$$

$$\frac{\partial p}{\partial t} + \frac{1}{2}\left\{\mathscr{L}_4 + \mathscr{L}_1\right\} + \frac{2\rho c^2 u}{r} + \frac{v}{r}\frac{\partial p}{\partial \theta} + \frac{\rho c^2}{r}\frac{\partial v}{\partial \theta} + \frac{\rho v c^2}{r\tan\theta} = 0, \tag{18}$$

7

$$\frac{\partial u}{\partial t} + \frac{1}{2\rho c}\left\{\mathscr{L}_4 - \mathscr{L}_1\right\} + \frac{v}{r}\frac{\partial u}{\partial \theta} + \frac{v^2}{r} + g\cos\theta = 0, \qquad (19)$$

$$\frac{\partial v}{\partial t} + \mathscr{L}_3 + \frac{v}{r}\frac{\partial v}{\partial \theta} + \frac{1}{r\rho}\frac{\partial p}{\partial \theta} + \frac{uv}{r} - g\sin\theta = 0, \qquad (20)$$

where each of the four $\mathscr{L}_i$ describes a characteristic wave mode, each with propagation speed λ_i. The terms proportional to $2u/r$ and $1/r\tan\theta$ are source terms due to the polar coordinates. c is the local speed of sound. The λ_i are defined by

$$\lambda_1 = u - c, \qquad \lambda_2 = \lambda_3 = u, \qquad \lambda_4 = u + c. \qquad (21)$$

The $\mathscr{L}_i$ are defined as

$$\mathscr{L}_1 = \lambda_1\left\{\frac{\partial p}{\partial r} - \rho c\frac{\partial u}{\partial r}\right\}, \qquad (22)$$

$$\mathscr{L}_2 = \lambda_2\left\{c^2\frac{\partial \rho}{\partial r} - \frac{\partial p}{\partial r}\right\}, \qquad (23)$$

$$\mathscr{L}_3 = \lambda_3\left\{\frac{\partial v}{\partial r}\right\}, \qquad (24)$$

$$\mathscr{L}_4 = \lambda_4\left\{\frac{\partial p}{\partial r} + \rho c\frac{\partial u}{\partial r}\right\}, \qquad (25)$$

Finite difference simulations of the Euler equations involve the following scheme: (1) calculation of spatial derivatives based on the solution at the current time step; (2) using these spatial derivatives in some form of the Euler equations to determine time derivatives; then (3) integrating the time derivatives to obtain the solution at the next time step. On boundary nodes equations 17 to 20 are solved. At any point in space, each characteristic wave mode $\mathscr{L}_i$ is described entirely by information downstream of that point determined by the corresponding characteristic wave speed λ_i.

If the characteristic wave $\mathscr{L}_i$ is propagating into Ω on Γ ($\lambda_i < 0$ at $r = R_D$), the information describing that wave mode is contained entirely outside the domain, and hence $\mathscr{L}_i$ must be specified by some artificial boundary condition (for example, $\mathscr{L}_i = 0$). If the characteristic wave is propagating out of the domain then it is entirely defined by information contained within the domain, in which case equations 22, 23, 24 or 25 may be used to define $\mathscr{L}_i$, based upon the solution within the domain. For example, a zero-velocity

boundary condition (a reflective boundary) on Γ is applied by computing $\mathscr{L}_4$ from its definition in equation 25, prescribing $\mathscr{L}_1 = \mathscr{L}_4$ and $\mathscr{L}_2 = \mathscr{L}_3 = 0$, and then solving equations 17 to 20 at that point.

Thompson [9] describes a 'non-reflecting' boundary condition as one in which all characteristic waves incoming to the domain are suppressed. To apply this boundary condition on Γ with subsonic flow, we compute $\mathscr{L}_4$ from its definition in equation 25 and prescribe $\mathscr{L}_1 = 0$. $\mathscr{L}_2 = \mathscr{L}_3 = 0$ if $u(b,t) \geq 0$, otherwise $\mathscr{L}_2$ and $\mathscr{L}_3$ are defined from equations 23 and 24. We then solve equations 17 to 20 at that point. Thompson [10] admits that there are many situations in which the correct solution does contain both outgoing and incoming characteristic waves, and demonstrates some of the limitations of this boundary condition.

3.2. Boundary conditions using the non-linear acoustic approximation

The NLAA yields a good approximation to the motion of an air gun bubble or underwater explosion provided it is not used in such close proximity to the bubble that the assumptions on which is founded are invalid. If an oscillating bubble is simulated on a finite domain of sufficient radius, then the approximate motion of the water outside the domain may be calculated using the NLAA based on the solution on the domain boundary. Furthermore, this approximate solution may then be used to provide boundary conditions for the finite volume simulation of the bubble.

The NLAA is only valid for problems with spherical symmetry, in regions where the density variation is small, and velocities are small compared with sound speeds. Consider again the domain Ω, defined by $0 \leq r \leq R_D$, bounded by Γ. Within Ω there may be an air gun bubble, an underwater explosion, or some other source, but R_D is large enough that on Γ the NLAA is valid. Within Ω there is no limit to flow speeds or directions. On R_D, $\lambda_1 < 0$ and $\lambda_4 > 0$. As such, $\mathscr{L}_1$ must be specified on the boundary from information based on the approximation to the exterior flow. The velocities in the water will sometimes be directed inwards and sometimes outwards. If $u(R_D, t) > 0$ then $\mathscr{L}_2$ and $\mathscr{L}_3$ can be calculated from equations 23 and 24. If $u(R_D, t) < 0$ then $\mathscr{L}_2$ and $\mathscr{L}_3$ must be specified from information based on the external flow. $\mathscr{L}_4$ will always be set by equation 25.

3.2.1. Prescription of $\mathscr{L}_1$

The results of equations 10 and 12 are passed back into the definition of $\mathscr{L}_1$ to obtain

$$\mathscr{L}_1 = \frac{\rho\,(u-c)}{r} \left\{ -\frac{1}{r}f' - \frac{1}{c}f'' + (u+c)\left(\frac{2}{r^2}f + \frac{2}{rc}f' + \frac{1}{c^2}f''\right)\right\}. \qquad (26)$$

Using the results of equations 13, 14 and 15 equation 26 becomes

$$\mathscr{L}_1 = \frac{\rho\,(u-c)}{r} \left\{ \frac{u^2}{2}\left(3 - \frac{u}{c}\right) + 2uc - \frac{p - p_\infty}{\rho_\infty}\left(1 + \frac{u}{c}\right) + \frac{u}{c}r\frac{\partial u}{\partial t}\right\}. \qquad (27)$$

We write

$$\mathscr{L}_1 = \frac{\rho\,(u-c)\,u}{c}\frac{\partial u}{\partial t} + \alpha_{\mathscr{L}_1}, \qquad (28)$$

where

$$\alpha_{\mathscr{L}_1} = \frac{\rho\,(u-c)}{r}\left\{\frac{u^2}{2}\left(3 - \frac{u}{c}\right) + 2uc - \frac{p - p_\infty}{\rho_\infty}\left(1 + \frac{u}{c}\right)\right\}. \qquad (29)$$

Equation 19 may now be expressed as

$$\frac{\partial u}{\partial t} + \frac{1}{2\rho c}\left\{\mathcal{L}_4 - \alpha_{\mathscr{L}_1} - \frac{\rho\,(u-c)\,u}{c}\frac{\partial u}{\partial t}\right\} + \frac{v}{r}\frac{\partial v}{\partial \theta} + \frac{v^2}{r} + g\cos\theta = 0. \qquad (30)$$

Equation 30 can be re-arranged to form

$$\frac{\partial u}{\partial t} + \frac{\frac{1}{2\rho c}\left\{\mathcal{L}_4 - \alpha_{\mathscr{L}_1}\right\} + \frac{v}{r}\frac{\partial v}{\partial \theta} + \frac{v^2}{r} + g\cos\theta}{1 - \frac{(u-c)u}{2c^2}} = 0 \qquad (31)$$

Equation 31 is solved to find $\frac{\partial u}{\partial t}$. Equation 28 is then used to calculate $\mathscr{L}_1$, which is passed to equations 17 and 18, and used to calculate $\frac{\partial \rho}{\partial t}$ and $\frac{\partial p}{\partial t}$.

3.2.2. Prescription of $\mathscr{L}_2$

When $u > 0$ on Γ, $\mathscr{L}_2$ may be determined from the definition in equation 23. When $u < 0$ on Γ, $\mathscr{L}_2$ must be determined based on the solution of the NLAA. The NLAA is based on the contradictory combination of assumptions of constant finite sound speed in an incompressible fluid. With the assumption of constant uniform density, equations 12 and 23 are used to obtain

$$\mathscr{L}_2 = -\rho u \left(\frac{2u}{r^3}f + \left(\frac{2u}{c} - 1\right)\frac{1}{r^2}f' + \left(\frac{u}{c} - 1\right)f''\right). \qquad (32)$$

10

Equations 13, 14 and 15 are substitued into equation 32 which becomes

$$\mathscr{L}_2 = \frac{\rho u^2}{r} \left[\frac{p - p_\infty}{c\rho_\infty} - 2u + \frac{u^2}{2c} \right] + \rho u \left(1 - \frac{u}{c} \right) \frac{\partial u}{\partial t}. \tag{33}$$

Once equation 31 has been solved, $\mathscr{L}_2$ is determined from equation 33, which is used in equation 17 to obtain $\frac{\partial \rho}{\partial t}$.

$\mathscr{L}_2$ describes the entropy at the boundary. An alternative approach is to state that the entropy is constant in the radial direction by setting $\mathscr{L}_2 = 0$. We find that the maximum relative error caused by this second approach is of the order of $10^{-3}\%$.

3.2.3. Prescription of $\mathscr{L}_3$

The NLAA is based on the polar and azimuthal components of velocity being zero on Γ. In a two-dimensional scheme, this may not be the case. However, as the NLAA makes no provision for determining the variation of polar velocities with radius, we make the most basic approximation possible, and state that the variation of polar velocity with radius is zero. Hence, if $u > 0$ on Γ, then $\mathscr{L}_3$ is determined from equation 22, otherwise $\mathscr{L}_3 = 0$. This assumption is equivalent to stating that there is no advection of transverse velocities through Γ.

3.2.4. Prescription of $\mathscr{L}_4$

Since the motion on Γ is always subsonic, $\mathscr{L}_4$ is defined by equation 25.

4. Computational Implementation

Numerical results are obtained by solving the Euler equations on a fixed domain, Ω, as in Section 3. The coordinate system is aligned with the polar axis pointing vertically upwards. In two dimensions with symmetry about the polar axis, the Euler equations may be written as

$$\frac{\partial \mathbf{U}}{\partial t} + \frac{\partial \mathbf{F}(\mathbf{U})}{\partial r} + \frac{\partial \mathbf{G}(\mathbf{U})}{\partial \theta} + \mathbf{S_r}(\mathbf{U}) + \mathbf{S_\theta}(\mathbf{U}) = \mathbf{D}(\mathbf{U}), \tag{34}$$

where

$$\mathbf{U} = \begin{bmatrix} \rho, & \rho u, & \rho v, & E \end{bmatrix}^T, \tag{35}$$

$$\mathbf{F} = \begin{bmatrix} \rho u, & \rho u^2 + p, & \rho u v, & u(E + p) \end{bmatrix}^T \tag{36}$$

and

$$\mathbf{G} = \left[\begin{array}{cccc} \rho v, & \rho u v, & \rho v^2 + p, & v\left(E + p\right) \end{array} \right]^T, \tag{37}$$

in which ρ, u, v, E and p are the density, radial velocity, polar velocity, total energy and pressure respectively. The source terms $\mathbf{S_r}$ and $\mathbf{S}_\theta$ are due to the polar coordinate system, and are given by

$$\mathbf{S_r} = \frac{2}{r} \left[\begin{array}{cccc} \rho u, & \rho u^2, & \rho u v, & u\left(E + p\right) \end{array} \right]^T \tag{38}$$

and

$$\mathbf{S}_\theta = \frac{1}{r \tan \theta} \left[\begin{array}{cccc} \rho v, & \rho u v, & \rho v^2, & v\left(E + p\right) \end{array} \right]^T. \tag{39}$$

The effects of gravity are accounted for by $\mathbf{D}$, defined by

$$\mathbf{D} = \left[\begin{array}{cccc} 0, & -\rho g \cos \theta, & \rho g \sin \theta, & -\rho g \left(u \cos \theta - v \sin \theta\right) \end{array} \right]^T, \tag{40}$$

where g is gravity, and $g = 9.81 m s^{-1}$. The equations are closed with a stiffened gas equation of state given by

$$p = \left(\gamma - 1\right) \rho e - \gamma p_c, \tag{41}$$

where $E = \rho e + \frac{1}{2}\rho u^2$. For air we have $\gamma = 1.4$ and $p_c = 0$, which is equivalent to the ideal gas equation of state. For water we use, typically, $\gamma = 7.0$ and $p_c = 3 \times 10^8$ Pa.

Two-phase flow simulations are achieved using a single phase finite volume Euler solver in combination with a ghost fluid method (GFM) to account for the interface.

4.1. Single phase Euler solver

The single-phase Euler solver is a dimensionally-split first order Godunov-type scheme (see, for example, [34, 35]). Spatial reconstruction is piecewise constant in each cell based on cell centre values $\mathbf{U}_{i,j}^n$, where i and j denote the spatial indices of the cell in the radial and polar directions respectively, and n denotes the time index. Riemann problems at the cell faces are then defined by $R_{i+\frac{1}{2},j} = R\left(\mathbf{U}_{i,j}^n, \mathbf{U}_{i+1,j}^n\right)$, and $R_{i,j+\frac{1}{2}} = R\left(\mathbf{U}_{i,j}^n, \mathbf{U}_{i,j+1}^n\right)$, and are solved using a Roe-average Riemann solver (due to [36]) to obtain HLLC fluxes $\hat{\mathbf{F}}_{i+\frac{1}{2},j}$ and $\hat{\mathbf{F}}_{i,j+\frac{1}{2}}$ (see [37]). Source terms due to the spherical coordinate system and gravity are accounted for using a first-order operator splitting procedure [26].

4.2. Ghost fluid method

Ghost fluid methods are a family of front-tracking methods for the simulation of multimedium flows with sharp interfaces, first developed by Fedkiw [38]. Ghost fluid methods provide a relatively simple way to model multifluid flows with sharp interfaces. We use a variation of the 'real GFM' of [39]. We omit the isobaric fix of [39], and modify only the ghost cells.

The air-water interface is tracked using a level set, ϕ, which is initialised as a signed distance function of the interface and updated according to the advection equation $\phi_t + u_{LS}\phi_r = 0$. Spatial derivatives of the level set are obtained with a weighted essentially non-oscillatory (WENO) spatial reconstruction scheme due to [40]. For one-dimensional simulations, the level set velocity, u_{LS}, is taken to be equal to the velocity of the interface, and hence no re-initialisation procedure is required. For two-dimensional simulations the level set velocity is set as the local fluid velocity, and the level set reinitialisation equation, $\phi_t = \operatorname{sgn}(\phi^0)(1 - |\nabla\phi|)$, where ϕ^0 is the solution to the level set equation before reinitialisation, is solved to retain the signed distance function. We use a scheme due to [41], which is first-order accurate over the whole domain, and second-order accurate in the vicinity of the interface. By construction the interface cannot lie outside the domain. For both level set equations we use a first order scheme for time integration.

4.2.1. Ghost fluid method in one dimension

In one dimension the ghost fluid method is applied as follows. At each time step the location of the interface is determined by finding the zero level set. The index of the cell with cell centre immediately to the left of the interface is denoted q. A two-fluid Riemann problem is constructed, defined by $R\left(\mathbf{U}_q^n, \mathbf{U}_{q+1}^n\right)$. The Riemann problem is solved using the two-fluid approximate Riemann solver of [36], to provide the left and right star states, denoted $\mathbf{U}_L^\star$ and $\mathbf{U}_R^\star$. The two-fluid domain, Ω is duplicated to create two one-fluid domains, Ω_1 and Ω_2. Ω_1 contains real cells where $\phi \leq 0$ $i \leq q$, and a band of ghost cells where $\phi > 0$ ($i \geq q+1$). Ω_2 is populated by real cells where $\phi > 0$ and a band of ghost cells where $\phi \leq 0$. The band of ghost cells is required to be a minimum thickness of 2 cells for first-order methods, with higher-order methods requiring more ghost cells. Properties in the one-fluid domains are denoted $\mathbf{U}_{i,\Omega_1}^n$ and $\mathbf{U}_{i,\Omega_2}^n$. The cells in the one-fluid domains are

populated according to

$$\mathbf{U}_{i,\Omega_1}^n = \begin{cases} \mathbf{U}_i^n & \text{if } i \leq q \\ \mathbf{U}_L^\star & \text{if } i \geq q+1 \end{cases} \tag{42}$$

$$\mathbf{U}_{i,\Omega_2}^n = \begin{cases} \mathbf{U}_R^\star & \text{if } i \leq q \\ \mathbf{U}_i^n & \text{if } i \geq q+1 \end{cases} \tag{43}$$

The single-phase Euler solver is now used to update each of the domains separately, yielding $\mathbf{U}_{i,\Omega_1}^{n+1}$ and $\mathbf{U}_{i,\Omega_2}^{n+1}$. The level set is updated, then the two one-fluid domains are recombined to the two-fluid domain according to

$$\mathbf{U}_i^{n+1} = \begin{cases} \mathbf{U}_{i,\Omega_1}^{n+1} & \text{if } \phi_i^{n+1} \leq 0 \\ \mathbf{U}_{i,\Omega_2}^{n+1} & \text{if } \phi_i^{n+1} > 0 \end{cases} \tag{44}$$

4.2.2. Ghost fluid method in two dimensions

We find that the version of the real GFM used in the one-dimensional simulations does not provide adequate stability as the interface becomes significantly warped in two-dimensional simulations. In two dimensions we use a variation, which is the same as for the one dimensional case, except that whilst densities and velocities are defined by the solution to a Riemann problem, pressures are extrapolated from the region containing air. This modification is based on the modified GFM of [42], and the argument that the motion is predominantly constrained by air pressures and water velocities. A comparison of both versions of ghost fluid method on one-dimensional problems provided similar results. To apply this version of the GFM in two dimensions, we perform the following steps.

1. Determine whether each cell is beside the interface, and if so label it an 'interface cell'. A cell, A, with indices i_A, j_A, is an interface cell if there is a cell, B, such that

$$i_A - 1 \leq i_B \leq i_A + 1, \tag{45}$$

$$j_A - 1 \leq j_B \leq j_A + 1, \tag{46}$$

and

$$\phi_A \phi_B \leq 0. \tag{47}$$

2. For every interface cell, A

14

(a) find the partner cell, B, which satisfies equations 45, 46 and 47, and minimises the angle between the level set normals of the two cells, by finding B which minimises $(1 - \nabla\phi_A \cdot \nabla\phi_B)$;

(b) determine the components of the velocity in directions normal and tangent to the interface, u_n and u_t, where the normal to the interface is positive in the direction from fluid 1 to fluid 2 for cells A and B;

(c) solve a Riemann problem defined by $R\left(\tilde{\mathbf{U}}^n_A, \tilde{\mathbf{U}}^n_B\right)$, where $\tilde{\mathbf{U}} = (\rho,\, u_n,\, u_t,\, p)^T$, obtaining star states $\mathbf{U}^\star_L$ and $\mathbf{U}^\star_R$. Find the components of the star state velocities in the radial and polar directions;

(d) use the star states of the Riemann problem to define the densities and velocities in the ghost cell, B, beside the interface. Copy the air pressures from the interface cell in the air region.

3. Extrapolate the primitive properties away from the interface in the ghost regions by advecting with the level set normal:

$$\frac{\partial \xi}{\partial \tau} + \text{sgn}\left(\phi\right) \nabla\phi \cdot \nabla\xi = 0, \tag{48}$$

for $\xi = \rho, u, v, p$. Equation 48 is solved with first order upwind discretisation of spatial derivatives and a first order Euler method for time integration.

4. Update the properties in each domain separately using the single-phase Euler solver, to obtain $\mathbf{U}^{n+1}_{\Omega_1}$ and $\mathbf{U}^{n+1}_{\Omega_2}$.

5. Update the level set one time step, obtaining ϕ^{n+1}.

6. Reconstruct the properties in the two-fluid domain according to the sign of the level set:

$$\mathbf{U}^{n+1}_{i,j} = \begin{cases} \mathbf{U}^{n+1}_{\Omega_1, i, j} & \text{if } \phi^{n+1}_{i,j} \leq 0 \\ \mathbf{U}^{n+1}_{\Omega_2, i, j} & \text{if } \phi^{n+1}_{i,j} > 0. \end{cases} \tag{49}$$

This completes the time-step.

4.3. Boundary conditions

The NLAA boundary condition is applied by updating a band of ghost cells on Γ using the characteristic boundary condition formalism as described in Section 3 and a first order method for time integration. A reflecting

15

boundary condition is applied at the origin. For the two-dimensional cases a reflecting boundary condition is also applied on the boundaries where $\theta = 0$ and $\theta = \pi$.

4.4. Limitations of the numerical scheme

Our investigations are carried out using a scheme which is first order in time and space. Higher-order schemes including a second-order MUSCL scheme [43] and a 5th-order WENO scheme [40] with third-order time integration [44] were investigated. We have found that a first-order scheme provides best results. We compare our results for a one-dimensional underwater explosion problem with results of other authors [33, 45]. We find that our results using a first order scheme closely match those in [33, 45], whilst higher-order methods lead to severely damped bubble oscillations. We believe this is due to the different momentum and energy fluxes through the interface when the GFM is used in conjunction with a numerical scheme based on a wide stencil.

A flaw in the current scheme is that the Euler equations in polar coordinates are not in conservative form, due to the geometric source terms. When the motion of the interface is in the radial direction the regions either side of the interface are subject to erroneously high or low energies, and the Rankine-Hugoniot conditions are not met at the interface. The obvious symptom of these errors is a pressure discontinuity at the interface (visible in Figure 3) which is proportional in magnitude to the radial interface speed and the grid size. This error is reduced by refining the computational mesh. This is an open problem, and one which the authors are currently investigating.

5. Numerical results in one dimension

We test our method on single-phase and two-phase test problems in one dimension. In all cases, the computational domain is defined by $0 \leq r \leq R_D$, and is made up of uniform cells of width δr, and subject to spherical symmetry. Test problems are run with a range of values for R_D and δr. All cases are run with a CFL number of 0.8.

For all one-dimensional test problems gravity is neglected and the largest value of R_D is chosen such that there is insufficient time during the simulation for errors caused by the boundary condition to propagate back into the region of interest. This provides us with what is effectively an 'ideal' boundary

condition, against which to test the NLAA boundary condition. We refer to these cases as 'large domain' or 'ideal' boundary condition cases.

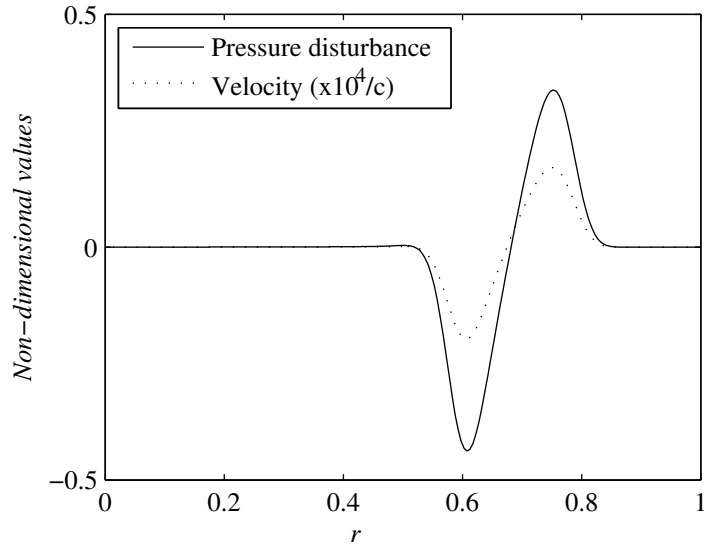## 5.1. Problem I - Travelling pulse in water

Figure 1: Problem I - Spatial pressure disturbance and velocity profiles for the outgoing pulse at time $t = 0.005$. Note that the velocity profile has been made non-dimensional with the local speed of sound and magnified by a factor of 10^4.

We first consider a single phase problem. The problem consists of a domain containing water initially at rest, with uniform density. The pressure of a sphere of water near the origin is increased relative to the surrounding water. These initial conditions produce a pulse which propagates outwards at the local speed of sound. Behind the outgoing pulse the velocity is zero and the pressure is uniform. The initial conditions are

$$(\rho,\, u,\, p,\, \gamma,\, p_c) = \begin{cases} (1,\, 0,\, 10,\, 7,\, 3000) & \text{if } 0 < r < 0.1, \\ (1,\, 0,\, 1,\, 7,\, 3000) & \text{if } 0.1 < r < R_D. \end{cases} \tag{50}$$

The simulation is run on a grid with $\delta r = 0.005$ for 400 time steps. We run the simulation on a domain with size $R_D = 1$ for our new artificial boundary condition (NLAA) and also for Thompson's [9] non-reflecting boundary condition (NR). We run the simulation on a domain with $R_D = 2$ to provide an ideal boundary condition. We calculate the pressure disturbance as
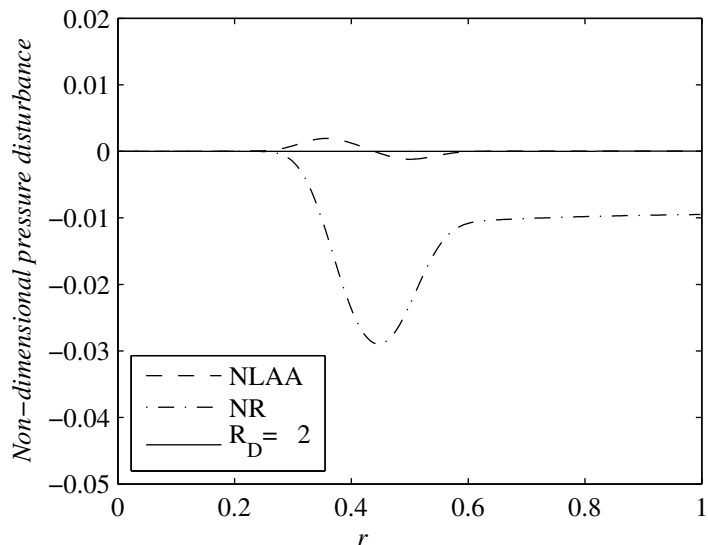
17

Figure 2: Problem I - The remaining pressure disturbances after the main pulse has left the domain due to different boundary conditions, at time $t = 0.011$. Solid line: large domain 'ideal' boundary condition. Dashed line: our non-linear acoustic approximation boundary condition. Dot-dashed: Thompson's [9] non-reflecting boundary condition.

the relative deviation of the absolute pressure from the initial pressure at the domain boundary (ie. $(p(r,t) - p_\infty)/p_\infty = p(r,t) - 1$). We make the velocity non-dimensional by multiplying by $10^4/c$, where c is the local speed of sound. Figure 1 shows the velocity and pressure disturbances due to the outgoing pulse. Figure 2 shows pressure disturbances, caused by the artificial boundary condition, propagating back towards the origin. It is apparent from Figure 2 that in this case the NLAA boundary condition outperforms the NR boundary condition: the disturbance which propagates inwards is of much smaller magnitude than that produced by Thompson's [9] boundary condition. The final pressure reached after a long time has elapsed is correct when using the NLAA boundary condition, but not when using the NR boundary condition. In this case the Mach number of the pulse as it impacts on the domain boundary is very low, at 1.5×10^{-5}. The strength of the pulse leaving the domain is very weak, and this case satisfies the assumptions on which the non-linear acoustic approximation is based. The amplitude of the spurious pulse caused by the boundary condition is approximately 350 times smaller than the amplitude of the pulse which propagates outwards.

18

5.2. Problem II-A.1 - Air gun bubble problem - early stages

We consider the problem of the bubble produced by a seismic air gun. This problem consists of an initially stationary bubble of air at high pressure in water. The initial conditions are:

$$(\rho,\, u,\, p,\, \gamma,\, p_c) = \begin{cases} (102,\, 0,\, 8.85 \times 10^6,\, 1.4,\, 0) & \text{if } 0 < r < 0.1, \\ (1000,\, 0,\, 1.77 \times 10^5,\, 7.0,\, 3 \times 10^8) & \text{if } 0.1 < r < R_D, \end{cases}$$
$$(51)$$

where all quantities are given in S.I. units. This problem is comparable with an air gun with a volume of 250 cubic inches, charged to a pressure of 2000 pounds per square inch at a depth of 7.7 metres. Air guns of this size and pressure are commonly used in industry. Note that the discrepancy in initial pressures - $8.85 \times 10^6 \text{Pa} \approx 1300 \text{psi}$ - is intentional, and is designed to account for the process by which air is released from the gun. We run the simulation for domain sizes, R_D, of 1 and 5 metres. In both simulations, a grid cell size of $\delta r = 2 \times 10^{-4}$ metres is used. The results with $R_D = 5$ are taken to be the ideal boundary condition case.
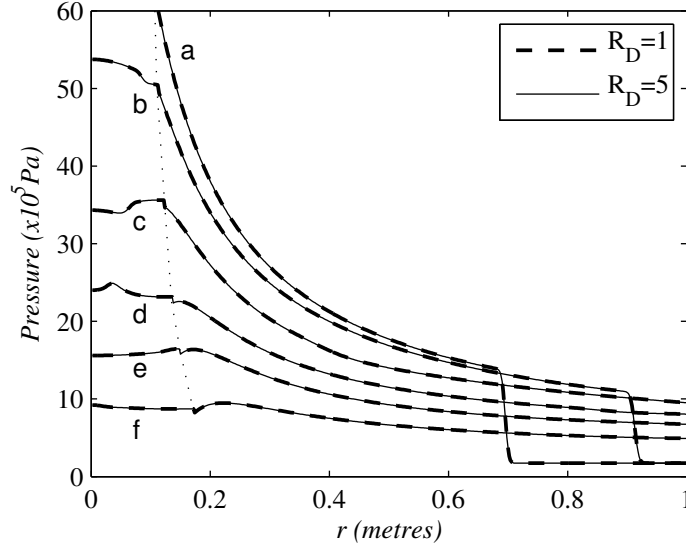

Figure 3: Problem II-A.1: Spatial pressure profiles at different times for domain sizes of $R_D = 1$ (NLAA BC) and $R_D = 5$ ('ideal' BC). (a) $t = 0.22$ms; (b) $t = 0.29$ms; (c) $t = 0.43$ms; (d) $t = 0.59$ms; (e) $t = 0.75$ms; (f) $t = 1.10$ms. The dotted line shows the location of the interface between air and water.

Figure 3 shows the pressure profiles at different times for the two domain sizes. Note the small discontinuity in pressure at the interface due to the ghost fluid method as discussed in Section 4.4. For both domain sizes, the pressure profiles match very closely and cannot be distinguished in Figure 3. As the outgoing pressure wave passes the domain boundary a disturbance due to the artificial boundary condition forms and propagates back into the domain. This disturbance causes density, velocity and pressure errors of $-3 \times 10^{-5}\%$, 0.007% and -0.04% respectively. That the error in pressure is negative and the error in velocity is positive implies that the artificial boundary condition is applying too weak a resistance at the boundary and is causing higher fluxes at the boundary than in the ideal case.

5.3. Problem II-A.2 - Air gun bubble - long run

We now consider the same problem as in the previous case but on longer time scales. We run the simulation for domain sizes, R_D, of 1, 2, 4, 8, 16 and 125 metres, with a cell size of $\delta r = 5 \times 10^{-3}$ metres. The simulation is run for 5×10^4 time steps, which corresponds to approximately 0.14 seconds, during which time the bubble undergoes two full oscillations. During the simulation, the maximum outgoing pressure wave impacts on the boundary in the $R_D = 125$ case; there is insufficient time for any disturbances to propagate back towards the origin as far as $r = 16$. We take the case of $R_D = 125$ as the case with ideal boundary condition with which to compare results obtained on smaller domains.

Figure 4 shows the time evolution of the interface position, R_{int}, and pressure, P_{int}, for $R_D = 1$. Figure 5 shows the magnitude in the relative error of the maximum interface interface position as R_D is varied. The results show third-order convergence of R_{int} with increasing R_D. P_{int} also shows third-order convergence. This convergence fails for $R_D = 16$ and 32, as the variation in density on R_D in these cases is of the same order of magnitude as machine precision.

For each value of R_D, the fluxes of the conservative properties are calculated at the domain boundary. The fluxes are also calculated at the same position for the case of $R_D = 125$. These fluxes are then integrated with respect to time to determine the total quantity of each conserved property which has left the domain. We then determine the relative errors in these cumulative fluxes, taking the case of $R_D = 125$ as a reference. Figure 6 shows the relative errors in the conservation properties of the boundary for differing domain sizes. Boundary conservation errors in energy match those in mass
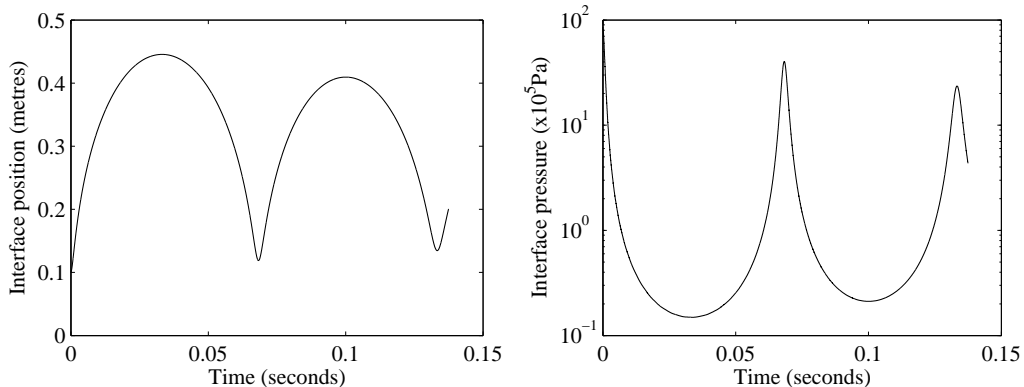
Figure 4: Problem II-A.2: Interface position and interface pressure variation as a function of time for $R_D = 1$.

to within 0.1% in all cases. Figure 6 shows a maximum error in boundary conservation after two full bubble oscillations (5×10^4 time steps) of approximately 10%. Figure 6 also shows a third-order convergence in boundary conservation errors as R_D is increased. When $R_D = 16$, variation in density at the domain boundary is of the same order of magnitude as machine precision errors, and hence the convergence characteristics of the smaller domains in Figure 6 appear not to hold.

This convergence rate is independent of mesh size, although errors due to the boundary conditions are reduced with finer mesh. We run the simulation for two domain sizes, $R_D = 1$ and $R_D = 2$ for a range of grid sizes, $\delta r = 5 \times 10^{-3}$, 2×10^{-3}, 1×10^{-3} and 3.33×10^{-3} metres, corresponding to 200, 500, 1000 and 3000 cells per metre respectively. With 3000 cells per metre, the simulation was run for 5×10^5 time steps. The relative error in interface position, $E_{R_{int}}$, and the relative error in interface pressure $E_{P_{int}}$ between the two domain sizes is calculated for each grid size. Table 1 shows the L_1 norm and the convergence rates for these errors. We find approximately first-order convergence of these errors with grid size.

5.4. Problem II-B.1 - Gaseous explosion in water - early stages

We consider an underwater explosion problem first studied by Flores and Holt [26]. Other authors have investigated this problem, using both Eulerian [28, 32, 33] and arbitrary Lagrangian-Eulerian [29, 30, 31] methods. This problem is similar to the problem of modelling a seismic air gun, but with a much greater initial pressure. The strength of the propagating shock in this
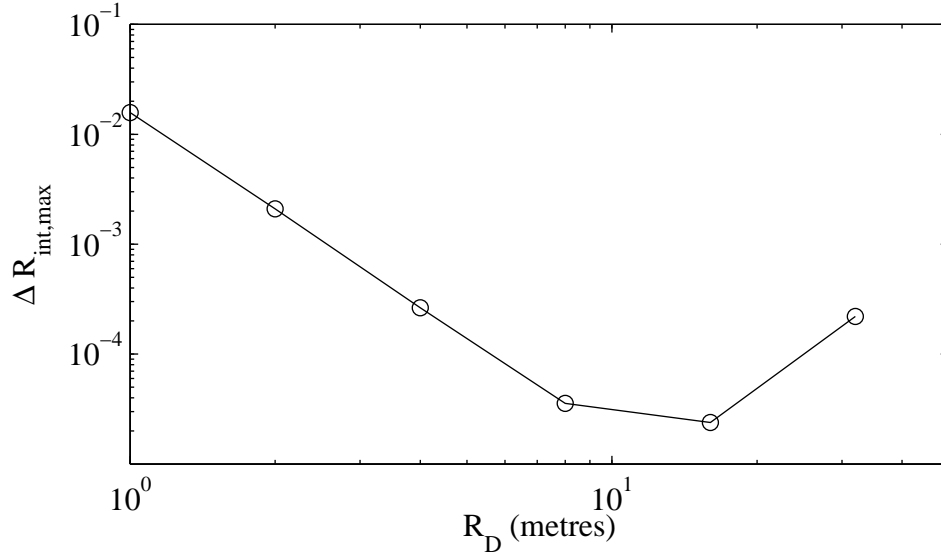
21

Figure 5: Problem II-A.2: Variation of the magnitude of the relative error in maximum interface position for different domain sizes. $\Delta R_{int,max} = |\max\left(R_{int,R_D}\right) - \max\left(R_{int,R_D=125}\right)| / \max\left(R_{int,R_D=125}\right)$.
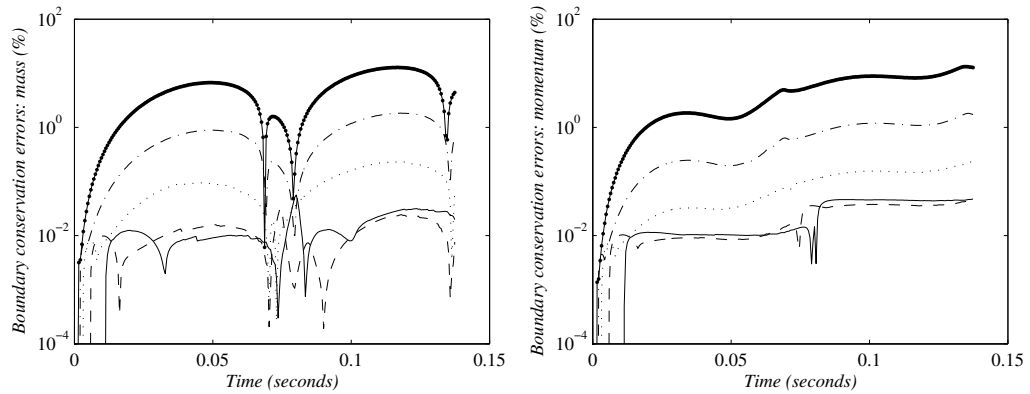

Figure 6: Problem II-A.2: Relative mass and momentum boundary conservation errors as functions of time for different values of R_D: $R_D = 1$ - solid line with points; $R_D = 2$ - dash-dot line; $R_D = 4$ - dotted line; $R_D = 8$ - dashed line; $R_D = 16$ - solid line.

22

δr (metres)	$E_{R_{int}}$	R_c	$E_{P_{int}}$	R_c
5×10^{-3}	7.05×10^{-3}		0.112	
2×10^{-3}	3.08×10^{-3}	0.916	0.047	0.958
1×10^{-3}	1.57×10^{-3}	0.981	0.024	0.991
3.33×10^{-4}	5.53×10^{-4}	0.946	8.3×10^{-3}	0.947

Table 1: Problem II-A.2: Relative errors due to boundary conditions and convergence rate with mesh refinement.

problem is greater than the non-linear acoustic approximation was designed for. As this problem is beyond the remit of the NLAA, it is a good test for the robustness of our method. The initial conditions are

$$(\rho,\, u,\, p,\, \gamma,\, p_c) = \begin{cases} (1.63,\, 0,\, 83810,\, 1.4,\, 0) & \text{if } 0 < r < 0.16, \\ (1.025,\, 0,\, 10,\, 5.5,\, 4921.15) & \text{if } 0.16 < r < R_D. \end{cases} \quad (52)$$

The simulation is run for domain sizes of $R_D = 1$ and $R_D = 5$, with $\delta r = 3.33 \times 10^{-4}$ metres in both cases. The case of $R_D = 5$ provides the ideal boundary conditions. The maximum Mach numbers occur at the interface, and are 0.55 in the bubble and 0.37 in the water. The maximum Mach number at $r = 1$ is 0.11.

Figure 7 shows the pressure profile at different times for both $R_D = 1$ and $R_D = 5$. Initially a shock wave propagations are from the interface into the water, and a rarefaction wave propagates into the bubble towards the origin. The shock wave is visible at about $r = 0.7$ in curve (a). As the rarefaction wave impacts on the origin it is reflected as a rarefaction wave, the pressure near the origin drops below the pressure in the rest of the bubble, and an inward propagating shock forms. This shock reflects of the origin and propagates outwards (it is visible at about $r = 0.1$ in curve (a)). Curve (b) shows this shock just prior to impacting on the interface. When it impacts on the interface, it is partially reflected back towards the origin, and partially transmitted out into the water (curve (c)). As the outgoing pressure wave impacts on the boundary a small disturbance forms and propagates back towards the origin (curves (c), (d) and (e)). The disturbance causes maximum errors of -15%, 1.5% and -0.1% in the pressure, velocity and density, respectively, at the boundary. The disturbance propagates in to the air-water interface, at which point it is partially reflected outwards, and partially transmitted into the bubble, where it grows in strength as it converges on the origin
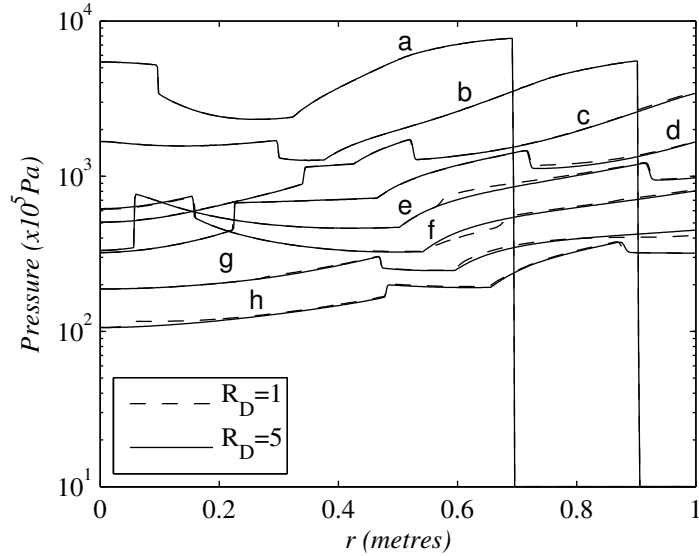
Figure 7: Problem II-B.1: Spatial pressure profiles at different times for domain sizes of $R_D = 1$ (NLAA BC) and $R_D = 5$ ('ideal' BC). (a) $t = 0.21$ms; (b) $t = 0.31$ms; (c) $t = 0.41$ms; (d) $t = 0.5$ms; (e) $t = 0.6$ms; (f) $t = 0.73$ms; (g) $t = 0.91$ms; (h) $t = 1.13$ms.

(curves (f), (g) and (h)).

5.5. Problem II-B.2 - Gaseous explosion in water - long run

We now test our method on the underwater explosion problem over a much greater run time, for one full bubble oscillation period. The initial conditions are the same as for the previous case. We now use a coarser grid, with $\delta r = 4 \times 10^{-3}$ metres. The simulation is run for domain sizes of $R_D = 3.5$, $R_D = 4$, $R_D = 6$, $R_D = 8$ and $R_D = 250$, for 1.25×10^5 time-steps. During the simulation the outgoing pressure wave reaches the boundary in all cases. When $R_D = 250$ spurious reflections from the boundary do not have time to propagate further inwards than $r = 100$. Hence the case of $R_D = 250$ is taken to be the ideal boundary condition with which to compare the performance of the boundary conditions on the smaller domains.

Figure 8 shows the time-evolution of the bubble radius and the interface pressure. These results are in good agreement with previous authors [29, 33]. The secondary oscillations ('internal bubble oscillations') present in the interface pressure in Figure 8 are due to pressure waves propagating across the bubble and interacting with the air-water interface, as described in the
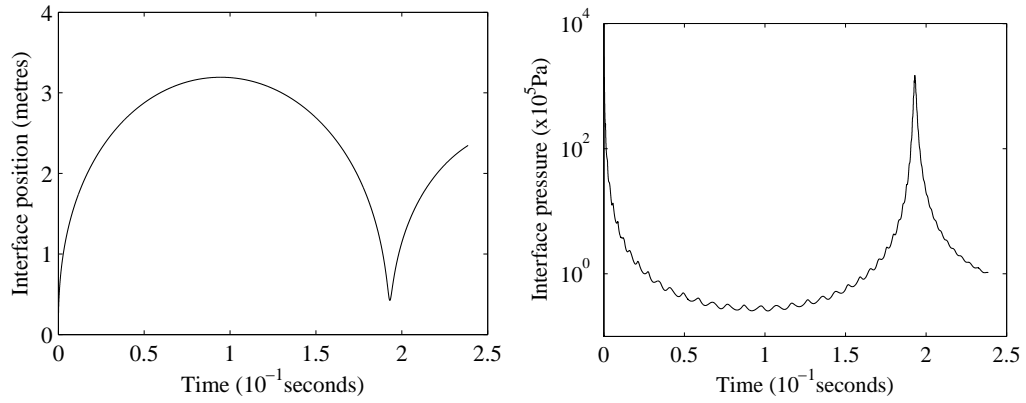
Figure 8: Problem II-B.2: Interface position and interface pressure variation as a function of time for $R_D = 4$.
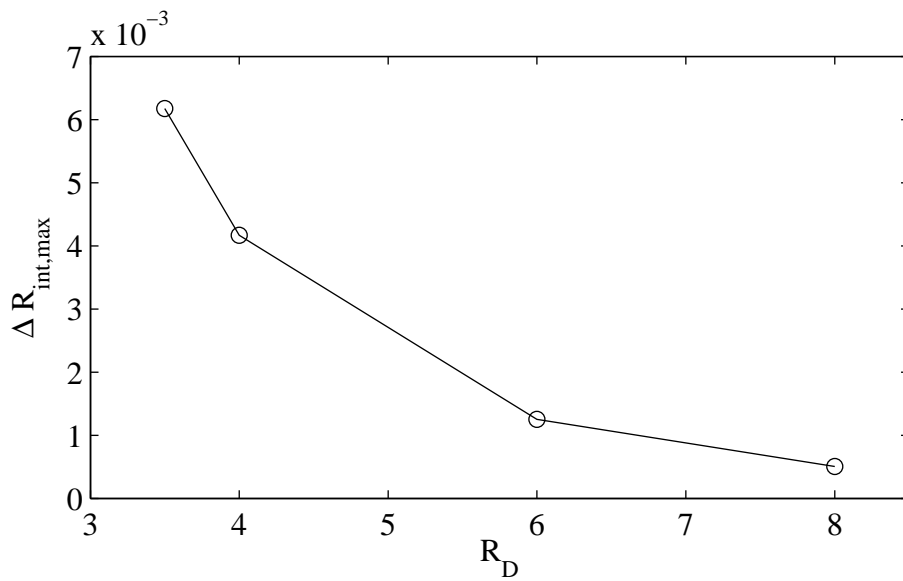

Figure 9: Problem II-B.2: Variation of the magnitude of the relative error in maximum interface position for different domain sizes. $\Delta R_{int,max} = |\max\left(R_{int,R_D}\right) - \max\left(R_{int,R_D=125}\right)| / \max\left(R_{int,R_D=250}\right)$.
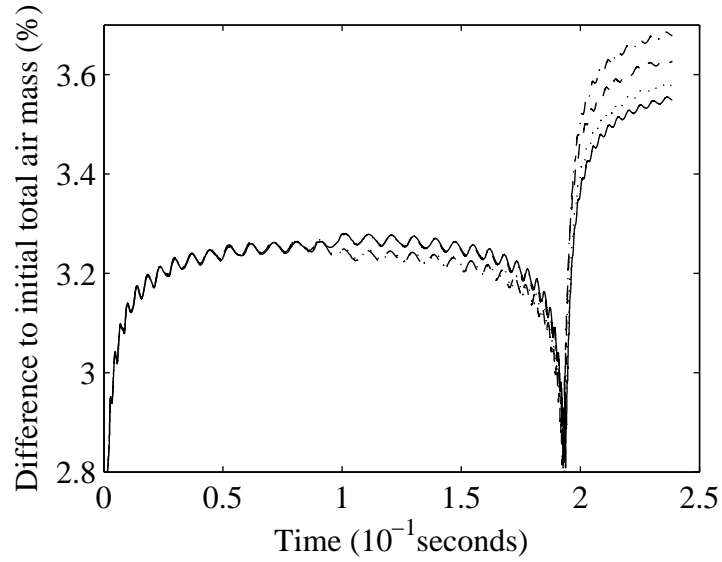
Figure 10: Problem II-B.2: Variation of air mass as a function of time for different values of R_D. Dashed line - $R_D = 4$; dash-dot line - $R_D = 6$; dotted line - $R_D = 8$; solid line - $R_D = 250$.
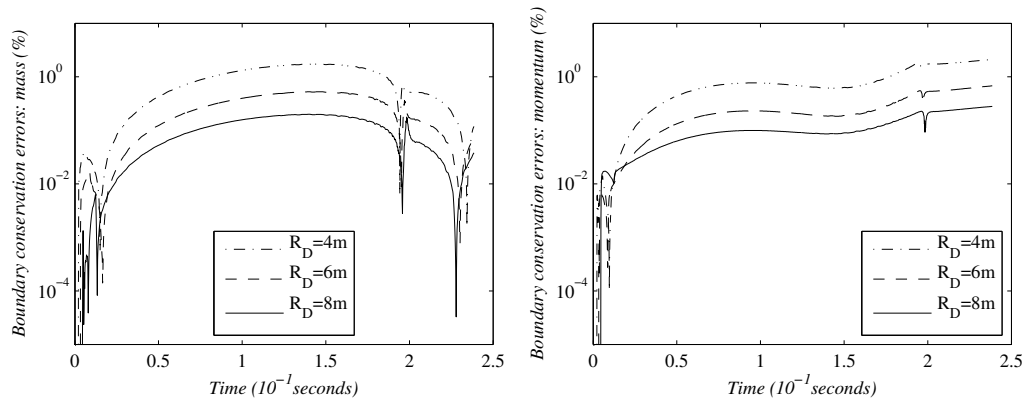

Figure 11: Problem II-B.2: Relative mass and momentum boundary conservation errors as a function of time for different values of R_D.

previous section. The maximum radius of the bubble during the simulation is 3.2 metres. The maximum Mach number at the domain boundary when $R_D = 4$ is 0.02, and initial shock which impacts on the boundary has a pressure ratio of 50. Figure 9 shows the magnitude of the relative error in maximum interface position for different values of R_D. The results show third-order convergence.

Figure 10 shows the time evolution of the error in the total mass of air in the bubble. The variation in Figure 10 of order 1% is due to the non-conservative properties of the ghost fluid method about the interface, and is unavoidable given the current numerical scheme, although it can be reduced with mesh refinement. The differences in mass conservation for different sized domains show no improved performance with larger domains. The variation between the traces in Figure 10 is due to the sensitivity of the conservation properties of the scheme to the time at which any disturbances from the domain boundary impact on the material interface. It must be noted that the interaction between the disturbance due to the boundary conditions and the wave inside the bubble has the ability to change the phase of the internal bubble oscillations significantly as the bubble collapses. As with previous test problems, we observe third-order convergence of interface position and pressure as R_D is increased.

Figure 11 shows the conservation errors in mass and momentum flowing out of the domain at R_D relative to the $R_D = 250$ case for each value of $R_D = 4$, 6 and 8. As in the previous cases, boundary conservation errors in energy matched those in mass to within 0.1%. These results show a third-order convergence for boundary conservation properties with increasing R_D. For the case of $R_D = 8$, the maximum errors in boundary conservation are of the order of 0.1%. This is a very good conservation property, given that the simulation has been run for such a large number of time steps.

We also run the simulation with $R_D = 3.21$, in which case R_D is 0.1% greater than the maximum bubble radius. In this case the results obtained match those expected from the convergence properties observed above. Recall that the simulation will break down if the interface moves outside the domain. We note that for the underwater explosion problem the minimum acceptable domain size is determined not by the performance of the boundary condition, but by the requirement that the domain is larger than the maximum bubble radius.

The NLAA boundary condition provides excellent results with regard to the large-scale motion of the bubble. Smaller scale motion, such as the

pressure waves oscillating within the bubble, are significantly affected by the boundary conditions, but they themselves have little effect on the bubble radius or interface pressure.

6. Results in two-dimensions

In our two-dimensional test problems, the computational domain is the region containing the points $0 \leq r \leq R_D$ and $0 \leq \theta \leq \pi$, and is split uniformly into cells with side lengths δr and $r\delta\theta$, where $\delta r = R_D/50$ and $\delta\theta = \pi/50$. In all cases, we set $R_D = 1$ and use a CFL number of 0.8.

6.1. Problem III-A.1 - Two-dimensional air gun bubble subject to a disturbance

We now simulate an air gun bubble as in Problem II-A, but the imposition of spherical symmetry is relaxed and the initial shape is subject to a small sinusoidal disturbance, η. For this problem we neglect gravity. The intitial conditions are given by

$$(\rho,\, u,\, p,\, \gamma,\, p_c) = \begin{cases} (102,\, 0,\, 8.85 \times 10^6,\, 1.4,\, 0) & \text{if } 0 < r < 0.1 + \eta, \\ (1000,\, 0,\, 1.77 \times 10^5,\, 7.0,\, 3 \times 10^8) & \text{if } 0.1 + \eta < r < R_D, \end{cases} \tag{53}$$

where all quantities are given in S.I. units. We set $\eta = 0.001 \sin(20\theta)$. Note that if we set $\eta = 0$ the initial conditions do not vary with θ, and the problem collapses to the one-dimensional problem. We run the simulation twice, with $R_D = 1$ and $R_D = 2$.

Figure 12 shows the shape of the bubble at different times during collapse, for the case of $R_D = 1$ (solid line) and $R_D = 2$ (dashed line). As the bubble expands outwards the disturbances to the interface do not grow, but are damped slightly, and so we do not show the shape of the bubble during the expansion phase. As the bubble collapses, the interface becomes unstable and the disturbances grow. This instability is a expression of Rayleigh-Taylor instability [46]. Our results agree with [47, 48], in which the changing form of the bubble surface during collapse can be seen in high-speed photographs of an air gun bubble. Due to the instability of the surface, the final shape of the bubble is highly sensitive to small changes during the earlier stages of oscillation. In Figure 12 the initial bubble shapes for the two cases are identical, whilst the final shapes of the two bubbles differ significantly. This is due to the small differences caused by errors due to the boundary condition.

If the model were used to study bubble surface instabilities, R_D, δr and $\delta \theta$ should be set such that grid converged results in terms of R_{int} and P_{int} are obtained.

Polar coordinate systems contain a singularity at the poles. It is well-known [49, 50, 51] that this singularity causes Rayleigh-Taylor instabilities to grow faster at the poles. This phenomenon is a numerical artefact of the discretisation. We observe this phenomenon in Figure 12, frames (F) to (H), where a long Rayleigh-Taylor finger protruding along the polar axis is clearly visible.

6.2. Problem III-A.2 - Two-dimensional air gun bubble under the influence of gravity

This final problem has the same initial conditions as problem II-A, but the imposition of spherical symmetry is relaxed, and the problem is subject to axi-symmetry about the polar axis. The initial conditions are adjusted to include the effects of gravity by augmenting pressure terms with the hydrostatic pressure, $p_{hydrostatic} = -\rho g r \cos \theta$. An effective bubble radius is obtained by calculating the volume of the bubble, and finding the radius of a sphere of that volume. The interface pressure is taken as the average pressure over the bubble surface.

Figure 13 shows the shape of the bubble as it collapses, both with (solid line) and without (dashed line) gravity. The case without gravity is spherically symmetric, and the bubble does not undergo any translation. We observe the bubble rising due to gravity, at a rate which is in agreement with previous numerical simulations [25]. As the bubble collapses, our results show a jet begins to form on the underside and pierce upwards through the bubble along the polar axis. This phenomenon is well known, and has been captured previously, for instance in [25, 52]. For most of the oscillation (the expansion phase, and frames (A) to (D) in Figure 13) the effects of gravity on the effective bubble radius and the bubble pressure are negligible. It is only during the latter stages of collapse that the translation and deformation of the bubble has a significant effect on the pressure far from the bubble. As discussed above, there is a singularity at the poles which increases the speed of growth of instabilities. In long run time simulations, these errors can evolve into axial jets [51]. We find that as the physical jet directed radially inwards approaches the origin, the unphysical jet forms in the opposite direction, and eventually leads to the breakdown of the simulation.
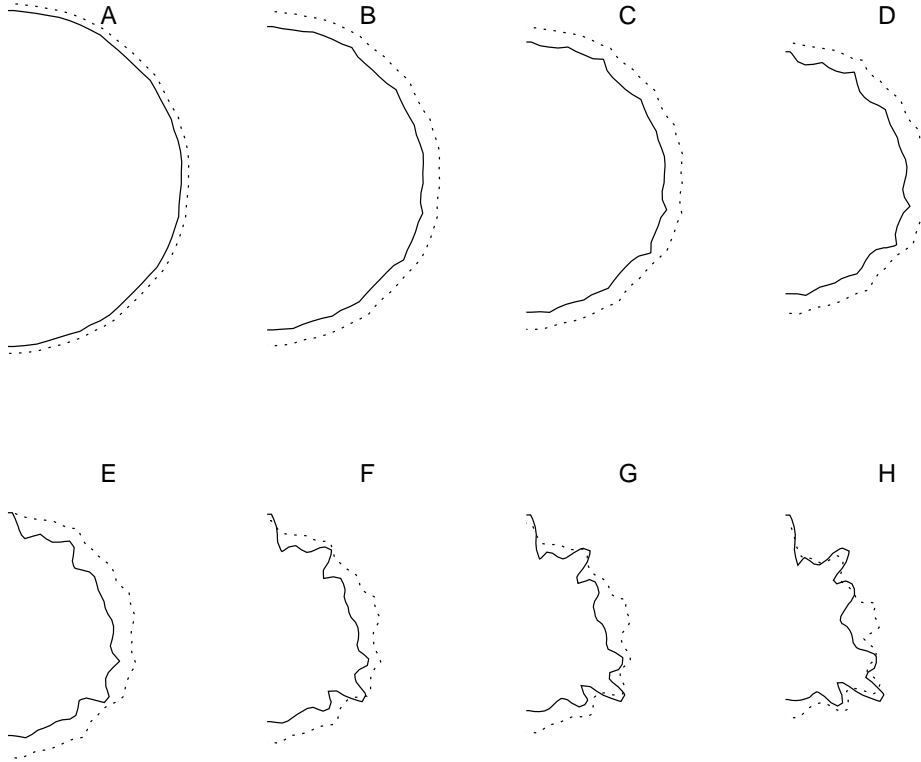
Figure 12: The shape of the bubble at different times during collapse, with $R_D = 1$. Gravity is neglected. The initial shape of the bubble is a sphere subject to a sinusoidal disturbance, $\eta = 0.001 \sin(20\theta)$. The solid line shows results with $R_D = 1$. The dashed line shows results with $R_D = 2$. (A) $t = 29.2$ms; (B) $t = 50.2$ms; (C) $t = 56.7$ms; (D) $t = 61.5$ms; (E) $t = 64.7$ms; (F) $t = 67.2$ms; (G) $t = 69.0$ms; (H) $t = 70.8$ms.

In its current form, the code would take an inordinately long time to simulate one oscillation of a two-dimensional bubble on a large domain, as we did for the one-dimensional results in Section 5. Hence we do not have an 'ideal boundary condition' result to allow the calculation of the absolute errors introduced by the boundary condition in two dimensions. Whilst much of the above discussion is unrelated to our boundary condition, this only serves to highlight its efficacy. The boundary condition allows two-dimensional simu-
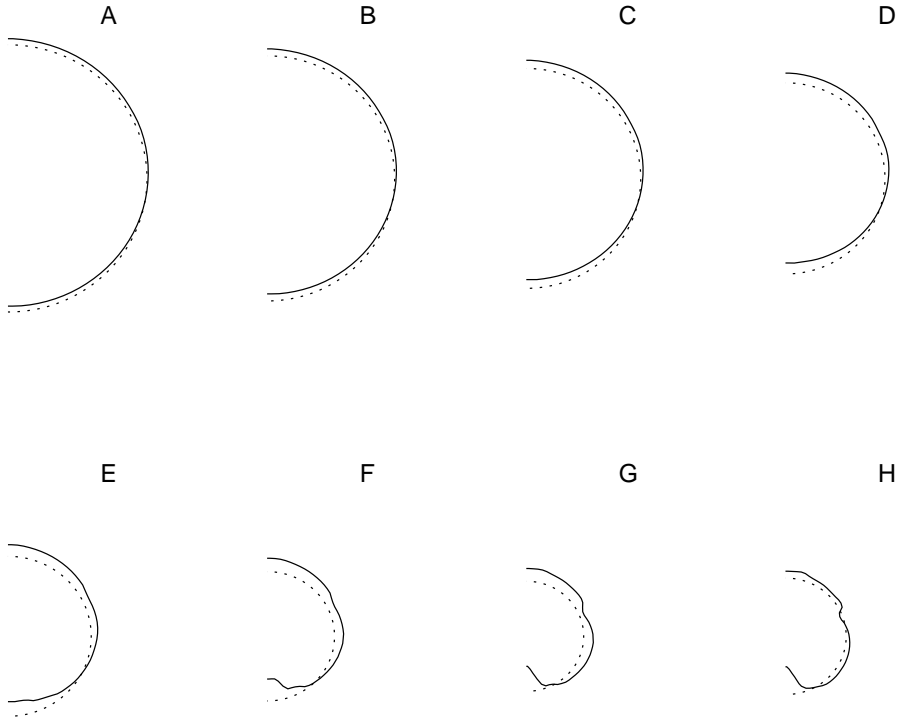
Figure 13: The shape and position of the bubble at different times during collapse, with $R_D = 1$, both with (solid line) and without (dotted line) gravity included. (A) $t = 56.8$ms; (B) $t = 59.8$ms; (C) $t = 62.7$ms; (D) $t = 65.3$ms; (E) $t = 67.7$ms; (F) $t = 69.9$ms; (G) $t = 71.8$ms; (H) $t = 73.6$ms.

lations of oscillating bubbles on small domains, at a reduced computational cost. This reduction in cost can facilitate research into more interesting details of bubble motion, such as surface instabilities and the formation of jets.

7. Conclusions

We have derived a new artificial boundary condition for numerical simulations of oscillating bubbles and similar problems on a finite domain. The

method is applicable when the problem is spherical in nature and close to spherically symmetric, and the motion at the domain boundary is of low Mach number (less than 0.1). The boundary condition is based on the non-linear acoustic approximation, developed for use in modelling seismic air guns. We use the non-linear acoustic approximation to calculate an approximate solution to the motion outside the domain based on the solution at the domain boundary. We apply boundary conditions by using the approximate solution to describe all characteristic waves incoming to the domain at the boundary. We implement our boundary condition in one- and two-dimensional two-phase Euler solvers. A Godunov-type scheme is used for single phase calculations, whilst the interface between phases is modelled using a ghost fluid method. The scheme is first-order accurate in space and time. We have tested our method on a range of one- and two-phase problems in one and two dimensions.

In one dimension, the method performs well, yielding accurate results for underwater explosion problems, even when the domain boundary is only slightly larger (0.1%) than the maximum bubble radius. A major benefit of the method is that it allows long run time (10^5 time steps with a CFL number of 0.8) simulations of such problems on a highly truncated domain, at a reduced computational cost. The method is robust, and capable of yielding good conservation properties (errors of less than 1%) over very long run times. Our two-dimensional results show that the boundary condition allows long run time simulations of axisymmetric oscillating bubbles provided computational domain extends some distance into the water such that the motion at the boundary is close to spherically symmetric. The value of our boundary condition to two-dimensional simulations is significant, as it permits complex aspects of bubble behaviour to be simulated at very small computational costs.

8. Acknowledgements

[1] D. Givoli, Non-reflecting boundary conditions, Journal of Computational Physics 94 (1991) 1–29. doi:10.1016/0021-9991(91)90135-8.

[2] T. Hagstrom, Radiation boundary conditions for the numerical simulation of waves, Acta Numerica 8 (1999) 47–106. doi:10.1017/S0962492900002890.

[3] S. V. Tsynkov, Numerical solution of problems on unbounded domains. A review, Applied Numerical Mathematics 27 (1998) 465–532. doi:10.1016/S0168-9274(98)00025-7.

[4] J.-P. Berenger, A perfectly matched layer for the absorption of electromagnetic waves, Journal of Computational Physics 114 (1994) 185–200. doi:10.1006/jcph.1994.1159.

[5] J.-P. Berenger, Three-dimensional perfectly matched layer for the absorption of electromagnetic waves, Journal of Computational Physics 127 (1996) 363–379. doi:10.1006/jcph.1996.0181.

[6] M. E. Hayder, F. Q. Hu, M. Y. Hussaini, Towards perfectly absorbing boundary conditions for euler equations, AIAA Journal 37 (1999) 912–918. doi:10.2514/2.810.

[7] T. Colonius, Modelling artificial boundary conditions for compressible flow, Annual Revew of Fluid Mechanics 36 (2004) 315–345. doi:10.1146/annurev.fluid.36.050802.121930.

[8] G. W. Hedstrom, Nonreflecting boundary conditions for nonlinear hyperbolic systems, Journal of Computational Physics 30 (1979) 222–237. doi:10.1016/0021-9991(79)90100-1.

[9] K. W. Thompson, Time dependent boundary conditions for hyperbolic systems, II, Journal of Computational Physics 89 (1990) 439–461. doi:10.1016/0021-9991(90)90152-Q.

[10] K. W. Thompson, Time dependent boundary conditions for hyperbolic systems, Journal of Computational Physics 68 (1987) 1–24. doi:10.1016/0021-9991(87)90041-6.

[11] J. W. S. Rayleigh, On the pressure developed in a liquid during the collapse of a spherical cavity, Philosophical Magazine 34 (1917) 94–99.

[12] H. Lamb, The early stages of submarine explosion, Philosophical Magazine 45 (1923) 257–265.

33

[13] C. Herring, Theory of the pulsations of the gas bubble produced by an underwater explosion, Office of Naval Research, Dept. of the Navy, 1941. doi:10.5962/bhl.title.47411.

[14] J. B. Keller, I. I. Kolodner, Damping of underwater explosion bubble oscillations, Journal of Applied Physics 27 (1956) 1152–1161. doi:10.1063/1.1722221.

[15] F. R. Gilmore, Collapse of a spherical bubble, Tech. Rep. No. 26-4, Hydrodyn. Lab., Calif. Inst. Tech. (1952).
URL `http://resolver.caltech.edu/CaltechAUTHORS:Gilmore_fr_26-4`

[16] M. S. Plesset, S. A. Zwick, A nonsteady heat diffusion problem with spherical symmetry, Journal of Applied Physics 23 (1952) 95–98. doi:10.1063/1.1701985.

[17] A. Prosperetti, M. S. Plesset, Vapour-bubble growth in a superheated liquid, Journal of Fluid Mechanics 85 (1978) 349–368. doi:10.1017/S0022112078000671.

[18] A. Prosperetti, A. Lezzi, Bubble dynamics in a compressible liquid. Part 1. First-order theory, Journal of Fluid Mechanics 168 (1986) 457–478. doi:10.1017/S0022112086000460.

[19] A. Lezzi, A. Prosperetti, Bubble dynamics in a compressible liquid. Part 2. Second-order theory, Journal of Fluid Mechanics 185 (1987) 289–321. doi:10.1017/S0022112087003185.

[20] A. Ziolkowski, A method for calculating the output pressure waveform from an air gun, Geophysical Journal of the Royal Astronomical Society 21 (1970) 137–161. doi:10.1111/j.1365-246X.1970.tb01773.x.

[21] A. Ziolkowski, Measurement of air-gun bubble oscillations, Geophysics 63 (1998) 2009–2024. doi:10.1190/1.1444494.

[22] A. Kucera, J. R. Blake, Approximate methods for modelling cavitation bubbles near boundaries, Bulletin of the Australian Mathematical Society 41 (1990) 1–44. doi:10.1017/S0004972700017834.

[23] M. C. Hooton, J. R. Blake, W. K. Soh, Behaviour of an underwater explosion bubble near a rigid boundary: theory and experiment, Fluid

Dynamics and Its Applications 23 (1994) 421–428. doi:10.1007/978-94-011-0938-3_40.

[24] J. R. Blake, G. S. Keen, R. P. Tong, M. Wilson, Acoustic cavitation: the fluid dynamics of non-spherical bubbles, Philosophical Transactions of the Royal Society of London A 357 (1999) 251–267. doi:10.1098/rsta.1999.0326.

[25] E. Cox, A. Pearson, J. R. Blake, S. R. Otto, Comparison of methods for modelling the behaviour of bubbles produced by marine seismic airguns, Geophysical Prospecting 52 (2004) 451–477. doi:10.1111/j.1365-2478.2004.00425.x.

[26] J. Flores, M. Holt, Glimm's method applied to underwater explosions, Journal of Computational Physics 44 (1981) 377–387. doi:10.1016/0021-9991(81)90058-9.

[27] M. Holt, Underwater explosions, Annual Review of Fluid Mechanics 9 (1977) 187–214. doi:10.1146/annurev.fl.09.010177.001155.

[28] J. P. Cocchi, R. Saurel, J. C. Loraud, Treatment of interface problems with Godunov-type schemes, Shock Waves 5 (1996) 347–357. doi:10.1007/BF02434010.

[29] A. R. Pishevar, R. Amirifar, An adaptive ALE method for underwater explosion simulations including cavitation, Shock Waves 20 (2010) 425–439. doi:10.1007/s00193-010-0275-x.

[30] G. Barras, M. Souli, N. Aquelet, N. Couty, Numerical simulation of underwater explosions using an ALE method. The pulsating bubble phenomena, Ocean Engineering 41 (2012) 53–66. doi:10.1016/j.oceaneng.2011.12.015.

[31] R. W. Smith, AUSM(ALE): A geometrically conservative arbitrary Lagrangian-Eulerian flux splitting scheme, Journal of Computational Physics 150 (1999) 268–286. doi:10.1006/jcph.1998.6180.

[32] T. G. Liu, B. C. Khoo, K. S. Yeo, The simulation of compressible multi-medium flow. I. A new methodology with test applications to 1D gas-gas and gas-water cases, Computers and Fluids 30 (2001) 291–314. doi:10.1016/S0045-7930(00)00022-0.

[33] X. Y. Hu, B. C. Khoo, N. A. Adams, F. L. Huang, A conservative interface method for compressible flows, Journal of Computational Physics 219 (2006) 553–578. doi:10.1016/j.jcp.2006.04.001.

[34] B. Einfeldt, On Godunov-type methods for gas dynamics, SIAM Journal of Numerical Analysis 25 (1988) 294–318.
URL http://www.jstor.org/stable/2157317

[35] M. J. Ivings, D. M. Causon, E. F. Toro, On Riemann solvers for compressible liquids, International Journal for Numerical Methods in Fluids 28 (1998) 395–418. doi:0.1002/(SICI)1097-0363(19980915)28:3¡395::AID-FLD718¿3.0.CO;2-S.

[36] X. Y. Hu, N. A. Adams, G. Iaccarino, On the HLLC Riemann solver for interface interaction in compressible multi-fluid flow, Journal of Computational Physics 228 (2009) 6572–6589. doi:10.1016/j.jcp.2009.06.002.

[37] E. F. Toro, M. Spruce, M. Speares, Restoration of the contact surface in the HLL-Riemann solver, Shock Waves 4 (1994) 25–34. doi:10.1007/BF01414629.

[38] R. P. Fedkiw, T. Aslam, B. Merriman, S. Osher, A non-oscillatory Eulerian approach to interfaces in multimaterial flows - the ghost fluid method, Journal of Computational Physics 152 (1999) 457–492. doi:10.1006/jcph.1999.6236.

[39] W. Wang, T. G. Liu, B. C. Khoo, A real ghost fluid method for the simulation of multimedium compressible flow, SIAM Journal of Scientific Computing 28 (2006) 278–302. doi:10.1137/030601363.

[40] R. Borges, M. Carmona, B. Costa, W. S. Don, An improved weighted essentially non-oscillatory scheme for hyperbolic conservation laws, Journal of Computational Physics 227 (2008) 3191–3211. doi:10.1016/j.jcp.2007.11.038.

[41] G. Russo, P. Smereka, A remark on computing distance functions, Journal of Computational Physics 163 (2000) 51–67. doi:10.1006/jcph.2000.6553.

[42] R. P. Fedkiw, Coupling an Eulerian fluid calculation to a Lagrangian solid calculation with the ghost fluid method, Journal of Computational Physics 175 (2002) 200–224. doi:10.1006/jcph.2001.6935.

[43] P. Colella, A direct Eulerian MUSCL scheme for gas dynamics, SIAM Journal on Scientific and Statistical Computing 6 (1985) 104–117. doi:10.1137/0906009.

[44] C.-W. Shu, S. Osher, Efficient implementation of essentially non-oscillatory shock capturing schemes, Journal of Computational Physics 77 (1988) 439–741. doi:10.1016/0021-9991(88)90177-5.

[45] H. Luo, J. D. Baum, R. Lhner, On the computation of multi-material flows using ALE formulation, Journal of Computational Physics 194 (2004) 304–328. doi:10.1016/j.jcp.2003.09.026.

[46] G. Taylor, The instability of liquid surfaces when accelerated in a direction perpendicular to their planes. I, Proceedings of the Royal Society of London A 201 (1950) 192–196. doi:10.1098/rspa.1950.0052.

[47] J. Langhammer, M. Landrø, High-speed photography of the bubble generated by an airgun, Geophysical Prospecting 44 (1996) 153–172. doi:10.1111/j.1365-2478.1996.tb00143.x.

[48] J. Langhammer, S. Graciet, I. Vik, M. Espeland, O. J. Lokberg, Holographic studies of the bubble generated by a seismic airgun, Journal of the Acoustical Society of America 97 (1995) 362–369. doi:10.1121/1.412321.

[49] J. Kane, D. Arnett, B. A. Remington, S. G. Glendinning, G. Bazan, E. Muller, B. A. Fryxell, R. Teyssier, Two-dimensional versus three-dimensional supernova hydrodynamic instability growth, The Astrophysical Journal 528 (2000) 989–994. doi:10.1086/308220.

[50] K. Kifonidis, T. Plewa, H. T. Janka, E. Muller, Non-spherical core collapse supernovae I. Neutrino-driven convection, Rayleigh-Taylor instabilities, and the formation and propagation of metal clumps, Astronomy and Astrophysics 408 (2003) 621–649. doi:10.1051/0004-6361:20030863.

[51] K. Kifonidis, T. Plewa, L. Scheck, H.-T. Janka, E. Muller, Non-spherical core collapse supernovae II. The late-time evolution of globally

anistropic neutrino-driven explosions and their implications for SN 1987 A, Astronomy and Astrophysics 453 (2006) 661–678. doi:10.1051/0004-6361:20054512.

[52] A. M. Zhang, S. P. Wang, G. X. Wu, Simulation of bubble motion in a compressible liquid based on the three dimensional wave equation, Engineering Analysis with Boundary Elements 37 (2013) 1179–1188. doi:10.1016/j.enganabound.2013.04.013.